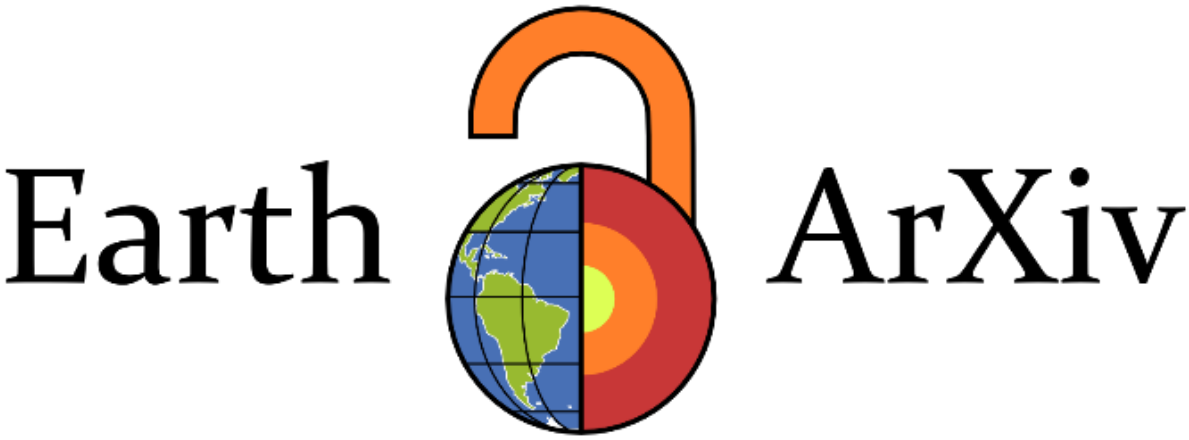

Homogenization of Elastic Wave Equation using Renormalization Group Theory

Authors: Bhaskar Illa[1],
Ajay Malkoti[2]*,
Shravan Hanasoge[1],
René-Édouard Plessix[3], and
Anu Chandran[4]

Affilitation: [1] Tata Institute of Fundamental Research, Colaba, Mumbai, India
[2] CSIR-National Geophysical Research Institute, Hyderabad-500007, India
[3] Shell Global Solutions International B.V., Amsterdam, Netherlands
[4] Shell International Exploration and Production, Inc.

Email*: ajaymalkoti@ngri.res.in, ajmalkoti@gmail.com

Abstract

Seismic waves traveling through the Earth interact with heterogeneities of all scales along their path. Generally, travel times associated with coarse-scale structures are of primary interest; however, fine-scale structures also influence the amplitude and travel time of all seismic phases. The distribution of fine-scale heterogeneities not only affects travel times but also impacts the observation of subsurface properties via these travel times. For instance, fine-scale isotropic heterogeneities in the medium, that may not be resolved in seismic imaging can induce extrinsic anisotropy on a coarser scale. Further, simulating seismic wavefield in a medium with all scales of heterogeneities requires a huge amount of computation, posing a significant challenge. To address these challenges, an upscaling technique based on Renormalization Group theory is proposed for the 2D elastic wave equation which gives an effective medium representation on coarser scale while preserving nature of wavefield. This approach is also helpful in understanding how seismic waves propagate through a medium containing fine-scale structures and how they are observed on the coarser scale. To validate the approach, different models were tested for various levels of upscaling. The waveforms and wavefields for both original and coarse-scale models matched well, demonstrating that the Renormalization Group theory-based upscaled medium effectively represents the fine-scale medium over the seismic frequency band.

Keywords: Upscaling, Renormalization Group theory, Elastic, Anisotropy, Homogenization

1 Introduction

The wave equation serves as a mathematical framework for understanding the propagation and interaction of seismic waves within the Earth with different geological structures. It holds significant importance in modern subsurface imaging techniques, viz., reverse time migration, and full waveform inversion (Baysal et al., 1983; Tarantola, 1984; Pratt et al., 1998). The true response results from the interaction of seismic waves with heterogeneities spanning all scales present within the medium. Now, there are two important aspects associated with it. First, we observe the medium properties with the finite resolution (i.e., using longer wavelengths), then the observed macroscopic (large scale) properties are different from the microscopic (small scale) properties. Our interest is to find the macroscopic representation of the medium with microscopic properties. Second is the computational aspect where to obtain the true response of the Earth one must include all scales of heterogeneities with the finest details, which makes the simulation extremely expensive. The macroscopic representation can reduce the computational burden significantly.

The macroscopic representation can be obtained using the Homogenization method (Bensoussan et al., 1978; Chammas et al., 2003; Gao et al., 2015). It gives a low wavenumber (macroscopic) representation of the medium properties and ensures that it does not alter the response of the Earth. The latter implies that the physical law governing the wave propagation yields the same wavefield for macroscopic representation as for the microscopic representations. In one of the first approach Backus (1962) computed equivalent macroscopic (anisotropic) medium for a stratified medium (elastic) comprising various layers. Since then, many approached has been developed under different names, such as upscaling, homogenization, coarsening, multiscale, computational micro-to-macro transition, etc. (Capdeville et al., 2010; Gold et al., 2000; Gibson Jr et al., 2014; Jordan, 2015; Vdovina et al., 2009; Fichtner and Hanasoge, 2017; Malkoti et al., 2022; Capdeville and Marigo, 2007; Guillot et al., 2010; Cupillard and Capdeville, 2018; Kormanikova and Kotrasova, 2022).

In this work, we will rely on the homogenization approach based upon the Renormalization group (RG) theory (Hanasoge, 2016; Hanasoge et al., 2017). The RG-based homogenization involves splitting the wave equation into low and high wavenumber parts. Since we are interested in low wavenumber representation, we incorporate the high wavenumber as a correction to it. This theory was extended for the 1D wave equation, but incurred a high computational cost due to the large size of the Fourier operator (Fichtner and Hanasoge, 2017). This cost increased many-fold in 2D/3D models, making upscaling unrealistic. To address the challenge of applying upscaling to higher-dimensional models, Malkoti et al. (2022), an expansion–truncation technique was proposed that enableed the feasible upscaling of the 2D acoustic wave equation. The focus of this work will be on extending this upscaling method for the elastic wave equation. We make use of a modified Fourier operator (Malkoti et al., 2022) for separating different quantities in low and high wavenumbers, which was applied to subdomains (with the expansion and truncation technique) to reduce the computational cost. We have tested the proposed RG-upscaling technique on two different fine scale elastic models. We validate results by matching the response obtained using the governing wave equation of the respective medium with microscopic details to that of a macroscopic (coarse-scale) model obtained after homogenization.

2 Theory

The propagation of a seismic wave in a general 2D-elastic medium is described by the equation of motion and stress-strain relation, given as the follows.

$$\rho\omega^2 \begin{bmatrix} u_1 \\ u_3 \end{bmatrix} = \begin{bmatrix} \partial_1 & 0 & \partial_3 \\ 0 & \partial_3 & \partial_1 \end{bmatrix} \begin{bmatrix} \sigma_{11} \\ \sigma_{33} \\ \sigma_{31} \end{bmatrix} \tag{1}$$

$$\begin{bmatrix} \sigma_{11} \\ \sigma_{33} \\ \sigma_{31} \end{bmatrix} = \begin{bmatrix} C_{11} & C_{13} & C_{15} \\ C_{31} & C_{33} & C_{35} \\ C_{51} & C_{53} & C_{55} \end{bmatrix} \begin{bmatrix} \epsilon_{11} \\ \epsilon_{33} \\ 2\epsilon_{31} \end{bmatrix} \tag{2}$$

Here, ω represents temporal frequency, ρ is the density of the medium, u_1 and u_3 represent displacement along the x- and z-axis, respectively, C_{ij} represents the stiffness tensor, σ_{ij} denotes stress component, and ϵ_{ij} denotes strain component, where $i, j \in \{x, z\}$.

To get the final expression, we substitute the expressions for different stresses (Equation 2) in the equation of motion (Equation 1) and expand the strain terms of displacements. On separating out the terms component wise, we get the expression as below:

$$\begin{aligned} -\omega^2 u_1 &= \rho^{-1}(\partial_1 C_{11}\partial_1 + \partial_1 C_{15}\partial_3 + \partial_3 C_{51}\partial_1 + \partial_3 C_{55}\partial_3)u_1 \\ &\quad + \rho^{-1}(\partial_1 C_{13}\partial_3 + \partial_1 C_{15}\partial_1 + \partial_3 C_{53}\partial_3 + \partial_3 C_{55}\partial_1)u_3 \end{aligned} \tag{3}$$

$$\begin{aligned} -\omega^2 u_3 &= \rho^{-1}(\partial_1 C_{51}\partial_1 + \partial_1 C_{55}\partial_3 + \partial_3 C_{31}\partial_1 + \partial_3 C_{35}\partial_3)u_1 \\ &\quad + \rho^{-1}(\partial_1 C_{53}\partial_3 + \partial_1 C_{55}\partial_1 + \partial_3 C_{33}\partial_3 + \partial_3 C_{35}\partial_1)u_3 \end{aligned} \tag{4}$$

The above equation requires accurate medium properties, capturing information at all scales, to simulate the wave propagation realistically. Now we try to upscale this equation using RG theory, for which we need to transform the above equations in terms of spatial frequencies or wavenumbers. The conventional Fourier operator typically returns wavenumber components in a mixed form. However, in this context, we require the wavenumbers in a sorted fashion, i.e., low and high wavenumbers separated along each axis. For that, a modified Fourier operator ($\hat{F}$) is created, which can be concisely represented as follows (Hanasoge et al., 2017; Malkoti et al., 2022).

$$\hat{F} = \begin{bmatrix} F_{ll} \\ \hline F_{lh} \\ F_{hl} \\ F_{hh} \end{bmatrix} = \begin{bmatrix} \hat{F}_l \\ \hat{F}_h \end{bmatrix} \tag{5}$$

Here, $\hat{F}_{ll}, \hat{F}_{lh}, \hat{F}_{hl}, \hat{F}_{hh}$, each represent the part of the Fourier operator that corresponds to a particular set of wavenumbers. For example, F_{ll} corresponds to the low wavenumbers along both axes, F_{lh} corresponds to the low wavenumbers along the first axis and high wavenumbers along the second axis, and similarly for others. Now, we segregate the operators into two parts- $\hat{F}_l$, which contains only low-wavenumber in both directions and $\hat{F}_h$, which contains high-wavenumber corresponding to any/both directions. It helps us to concentrate on the $\hat{F}_l$ for which the cut-off wavenumber is specified by the user.

Now, we will use this modified Fourier operator to project the wave equations (3) and (4). Before that, we have a look at projections of some basic entities, such as- partial derivative, material parameter (e.g. ρ, λ, μ, etc.), and particle motion u_i. Since we are using a discretized model, the derivative, material parameter, and motion can be represented as $\partial_i \to D_i$, $m \to M$, respectively.

Transforming the equations (3) and (4) requires application of $\hat{F}$ on both sides and inserting the $\hat{F}\hat{F}^{-1}$ between entities. It is very similar to the way presented in (Hanasoge, 2016; Malkoti et al., 2022). In the process, we need to calculate the following quantities.

$$\text{Wavefield:} \qquad \hat{F}\,U_i = \begin{bmatrix} \hat{U}_{L_i} \\ \hat{U}_{H_i} \end{bmatrix} \tag{6}$$

$$\text{Derivative:} \qquad \hat{F}\,D_i\hat{F}^{-1} = \begin{bmatrix} \hat{K}^i_L & 0 \\ 0 & \hat{K}^i_H \end{bmatrix} \tag{7}$$

$$\text{Material parameter:} \qquad \hat{F}\,M\hat{F}^{-1} = \begin{bmatrix} M_\alpha & M_\beta \\ M_\gamma & M_\delta \end{bmatrix} \tag{8}$$

In material parameters, subscripts α, β, γ, and δ are used to indicate elements of the partitioned matrix obtained using $\hat{F}\,M\hat{F}^{-1}$. We can use the above-derived expressions to project the elastic wave equation. We also observe that equations (3) and (4) contain some frequently occurring terms with a common structure shown below:

$$\rho^{-1}\partial_i C_{ij}\partial_j = BD_iMD_j \tag{9}$$

Here, B represents buoyancy (the inverse of density). It will be advantageous to obtain the projected form for such terms, in the generalized manner, and that can be utilized readily to derive the solution. The equations derived above for wavefield, derivative, and material parameter equations (6) to (8) can be used for this purpose.

$$\begin{aligned} &\hat{F}\,B\hat{F}^{-1}\hat{F}\,D_i\hat{F}^{-1}\hat{F}\,M\hat{F}^{-1}\hat{F}\,D_j\hat{F}^{-1} \\ &= \begin{bmatrix} B_\alpha & B_\beta \\ B_\gamma & B_\delta \end{bmatrix} \begin{bmatrix} \hat{K}^i_L & 0 \\ 0 & \hat{K}^i_H \end{bmatrix} \begin{bmatrix} M_\alpha & M_\beta \\ M_\gamma & M_\delta \end{bmatrix} \begin{bmatrix} \hat{K}^j_L & 0 \\ 0 & \hat{K}^j_H \end{bmatrix}, \qquad (10) \\ &= \begin{bmatrix} B_\alpha & B_\beta \\ B_\gamma & B_\delta \end{bmatrix} \begin{bmatrix} \hat{K}^i_L M_\alpha \hat{K}^j_L & \hat{K}^i_{LL} M_\beta \hat{K}^j_H \\ \hat{K}^i_H M_\gamma \hat{K}^j{}_L & \hat{K}^i_H M_\delta \hat{K}^j_H \end{bmatrix}, \qquad (11) \\ &= \begin{bmatrix} \hat{M}^{ij}_\alpha & \hat{M}^{ij}_\beta \\ \hat{M}^{ij}_\gamma & \hat{M}^{ij}_\delta \end{bmatrix}. \qquad (12) \end{aligned}$$

Now we come back to the projection of the wave equation equation (3). We see that the projection of each component yields all right-hand terms as the matrices shown in equation (12).

To simplify the representation, we represent them as an equation in the following format.

$$\omega^2 U_L = AU_L + BU_H\,, \tag{13}$$

$$\omega^2 U_H = CU_L + DU_H\,. \tag{14}$$

Generally, the impact of fine-scale structures in the medium is expected to be more pronounced on high-wavenumber components of the displacement compared to the low-wavenumber components. Consequently, our main aim is to derive a new equation that exclusively involves the low-wavenumber components of the wavefield, which are predominantly influenced by the smooth, low-wavenumber structure of the medium. In this regard, solving the above latter equation $(\omega^2 - D)U_H = CU_L$, which can be substituted back in the first equation, yielding the following.

$$\omega^2 U_L = [A + B(\omega^2 - D)^{-1}C]U_L\,. \tag{15}$$

Now it can be seen that the above equation is somewhat similar to the wave equation, except for the part where the ω term appears on the right-hand side. Owing to the low-wavenumber approximation, (Malkoti et al., 2022) we can approximate it by assuming $\omega \approx 0$. The rest of the part is to compare the coefficients and find an equivalent upscaled material parameters.

3 Numerical Tests

We demonstrate the application of the RG theory-based upscaling approach on field log data and an anticline model, all of which are elastic in nature. For that purpose, we have followed the workflow shown in Figure 1. First, we start with the given fine-scale elastic model which contains variation at all scales. The seismic response of this elastic medium is obtained through numerical simulations. Next, we derive a coarse-scale (upscaled) representation of the medium using the proposed RG theory, which inherently accounts for anisotropy. The seismic response of this anisotropic medium is also generated through numerical simulations. The numerical implementation of RG-based up-

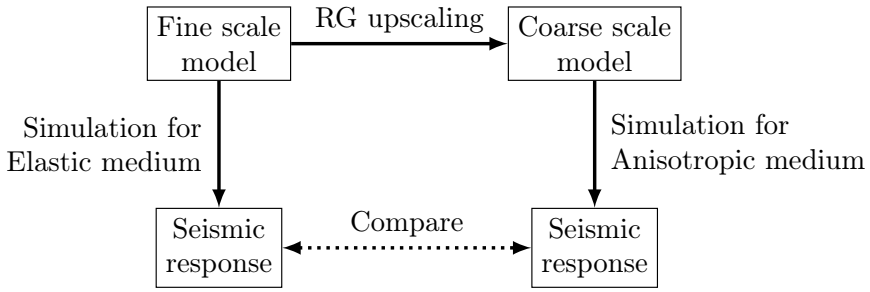

Figure 1: The figure gives a bird's-eye overview of the upscaling process.

scaling requires dividing the complete domain into smaller subdomains to reduce computational costs. To mitigate artifacts at subdomain boundaries, we adopted the expansion and truncation technique outlined by (Malkoti et al., 2022). For example, for upscaling a region for $\sigma = 2$, it requires extending each subdomain by 8 nodes in each direction, carrying out upscaling, and then finally 2 nodes were truncated. The portion of the upscaled model that remains after truncation is used for further analysis.

We employed the anisotropic wave equation Equations (1) and (2) to simulate wave propagation in both fine-scale (elastic isotropic) and RG-based upscaled (anisotropic) 2D models. The simulation for isotropic elastic medium were performed using FDwave package (Malkoti et al., 2018) which uses a staggered grid approach and the vectorized derivative scheme for carrying out the simulation. The simulation for the anisotropic medium simulations were performed using the rotated staggered grid (RSG) scheme (Saenger et al., 2000; Zhang and Schmitt, 2025), which is important for calculating the derivatives properly. We used the full upscaled stiffness tensor in the anisotropic case, which avoids redundant floating-point operations and improves computational efficiency. A velocity-stress formulation with a space order of 16 was adopted consistently across all simulations. Wave excitation was modeled using a broadband Ricker wavelet source located near the surface at the center of the model, with receivers distributed along the top surface. The maximum frequency content of the Ricker wavelet is approximated as $f_{\max} \approx 1.637 \times f_0$ (Wang, 2015), where f_0 is the central frequency; the minimum wavelength ($\lambda_{\min} = V_{\min}/F_{\max}$) of the medium was calculated using the lowest velocity ($V_{\min}$) in the model and the maximum frequency.

3.1 Hempens model

The geophysical borehole data represent the real Earth at a very fine resolution. This information can be used to analyze how the fine-scale earth properties are observed at the seismic scale of resolution. We have used the data from the HPS-01 borehole, Hempens field, Netherlands, which was operated by Vermilion Oil and Gas Netherlands B.V. We have used the log values in the depth interval ranging from 1160 m to 1920 m, with a sampling rate of 0.15 m. The primary lithological

formations within this depth range include chalk, alternating layers of chalk and chalky limestone, marl, sandstone, and claystone. The P-wave velocities range from 2514 m s^{-1} to 5750 m s^{-1}, while the S-wave velocities vary between 988 m s^{-1} and 2976 m s^{-1}, as shown in Figure 2.

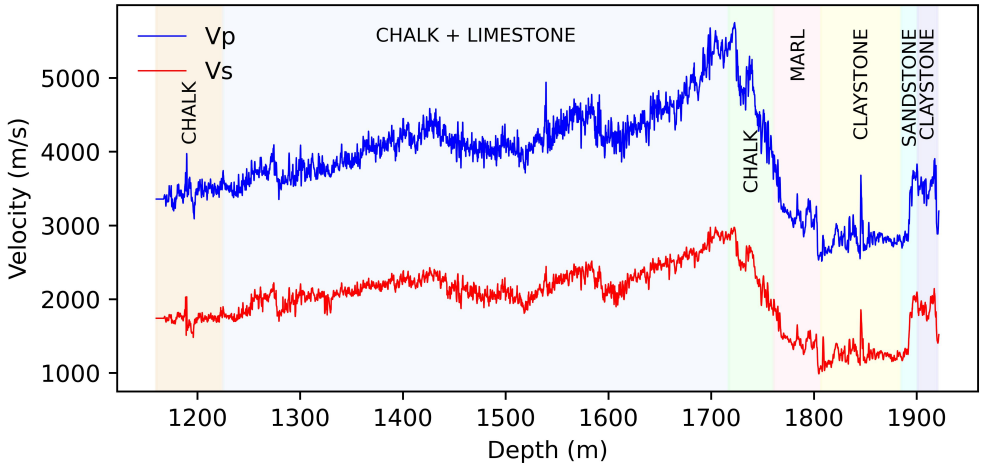

Figure 2: P-wave and S-wave velocities derived from field sonic log data for the borehole HPS-01, Hempens field, Netherlands.

We constructed a 1.5D elastic medium model from geophysical borehole log data and upscaled it using renormalization group (RG) theory with coarsening ratios $\sigma = 4$ (2^2) and $\sigma = 8$ (2^3). The resulting coarse models have grid spacings of 0.6 m and 1.2 m, respectively, with the larger coarsening ratio yielding a smoother representation. A comparison of the stiffness coefficients for the fine-scale medium and the RG upscaled mediums are shown in the Figure 3. Its upscaled values are in agreement with the fine-scale values, showing the averaging of the values and thereby shifting the wavenumber content to the lower side. The values are also compared with the Backus averaged model, which also gives the effective stiffness coefficients for a stacked layer elastic model. Backus averaging provides a well-established theoretical framework for computing effective medium properties in layered media (**see Appendix**). The Backus average is generally carried out over a length, L, given by–

$$L = \alpha \frac{v_{\min}}{f_0},$$

where α is a constant (generally taken as 0.1), $v_{\min}$ is the minimum wave speed, and f_0 is the dominant frequency. Figure 3 illustrates that RG-upscaled models with $\sigma = 4$ and $\sigma = 8$ retain higher-wavenumber content compared to the Backus-averaged model. However, the $\sigma = 8$ model appears smoother, with reduced high-wavenumber details relative to $\sigma = 4$. This difference in the wavenumber content of model can be partially attributed to the higher length of Backus averaging (arithmetic/harmonic) and partially to the correction term $(B(\omega^2 - D)^{-1}C)$ (equation (12)). This term was primarily responsible for incorporating the higher wavenumbers into the low-wavenumber model, which is generally similar to a spatial averaging filter. The fine-scale model contains the fastest spatial variations along depth. Upscaling generally reduces high-wavenumber content of the model. The RG-based models preserve more variability than the Backus-averaged model, with $\sigma = 4$ retaining more detail than the smoother $\sigma = 8$, while the Backus model remains dominated by low wavenumbers.

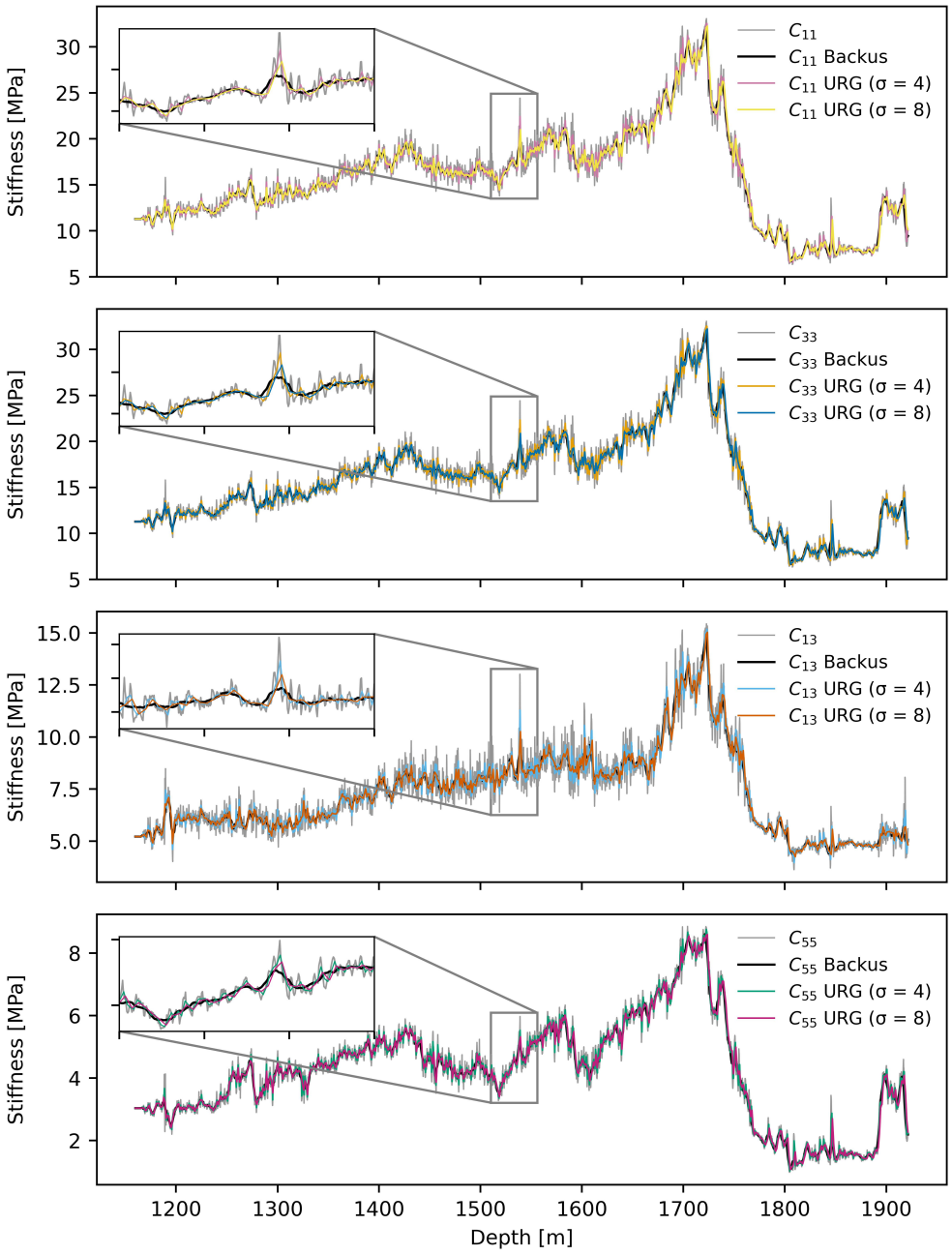

Figure 3: Superposition of stiffness coefficients C_{11}, C_{33}, C_{13}, and C_{55} derived from RG-based upscaling ($\sigma = 4$ and 8), Backus averaging (in black), and direct calculation from velocity profiles (in gray). The figure in the inset shows the enlarged part of the values to differentiate between them.

The Backus test gives us a sense of comparison but does not exactly justify whether the upscaling has been carried out in its true sense that upholds its definition. For that purpose, we have to simulate the seismogram on the given fine-scale medium and compare it with its upscaled-version (coarse-scale medium). We have carried out the seismic simulations for both fine-scaled (elastic) and coarse-scaled (anisotropic) media. These models were discretized on a rotated staggered grid,

enabling fourth-order spatial accuracy while minimizing dispersion errors, particularly in anisotropic media (Zhang and Schmitt, 2025). For both cases, we have used a Ricker wavelet with a central frequency of $f_0 = 40\,\text{Hz}$ as a source, which was placed at the laterally center of the model, near the surface. The grid spacing was 0.15 m for the fine-scale model and 0.6 m ($\sigma = 4$) or 1.2 m ($\sigma = 8$) for the coarse-scale models. The time step was selected to satisfy stability and dispersion constraints, with values of 0.01 ms for the fine-scale model, 0.04 ms for the upscaled model ($\sigma = 4$), and 0.08 ms for the upscaled model ($\sigma = 8$), ensuring a CFL number below 0.5. As a result, the upscaled models require 4 and 8 times fewer time steps than the fine-scale model, proportionally reducing computational cost and providing a substantial efficiency gain.

The top surface was enforced to be a free surface, where vertical tractions were made zero at the air-solid interface using the imaging condition (Vidale and Clayton, 1986). The method requires adding two extra nodes, called ghost rows/nodes, at the top edge of the model, which is the same for wave simulation in the fine-scale as well as for the upscaled model. A few extra node layers were used to absorb the reflections at all edges of the model, except the top. The number of absorbing layers was the same for wave simulation in the fine-scale as well as for the upscaled model. All other parameters were kept the same for the fine scale and the upscaled/coarse medium.

The output of the simulation can be compared component-wise for the full wavefield. Snapshots of the horizontal (U) and vertical (V) particle motion in the fine-scale and upscaled models are shown in Figure 4. The fine-scale model exhibits detailed high-wavenumber variations, including a prominent downward-propagating parabolic wavefront and scattered energy in both U and V components. The upscaled model ($\sigma = 4$) retains the overall wavefield structure but introduces noticeable smoothing that suppresses fine-scale oscillations while preserving the main wavefront geometry and amplitude distribution. This smoothing becomes more pronounced for $\sigma = 8$, producing a more homogenized appearance while still capturing the essential propagation features. Such progressive reduction in detail is a direct consequence of the upscaling process, which averages out sub-wavelength heterogeneities and enables simulations on coarser grids (1250×1250 for $\sigma = 4$, 625×625 for $\sigma = 8$) without significant loss of low-wavenumber information.
For a more detailed comparison, we examine the seismograms (U and V components) recorded at the surface, shown in Figure 5. The fine-scale model traces (black) capture phases associated with the layered lithologies. The upscaled $\sigma = 4$ traces (cyan) closely overlap with the reference, exhibiting only minor deviations in phase and amplitude. The upscaled $\sigma = 8$ traces (red) also reproduce the main arrivals but show slight mismatches at larger offsets and later times, including amplitude attenuation and small phase shifts. These discrepancies reflect the stronger smoothing effect of averaging sub-wavelength heterogeneities on the coarser grid. Overall, both U and V components confirm that the RG-based upscaling successfully reproduces the fine-scale seismic response on coarser grids, with differences primarily due to the loss of high-wavenumber content.

The upscaling process can be carried out up to a certain coarsening level only. This limitation is introduced by the derivative operator, whose accuracy is limited due to numerical dispersion. For example, the derivative operator requires more than 13 grid points per wavelength to have the grid dispersion below 5% (Levander, 1988). In this case, the maximum coarsening value σ is defined as the ratio of maximum allowed size divided by the actual sampling size. In the present work we have carried out upscaling of the log that was sampled at 0.15 m. Let us take an example of a Ricker wavelet of 50 Hz, which has a maximum frequency content of 81.85 Hz (Wang, 2015). In the given model the minimum wavelength turns out to be ∼12 m. The derivative operator requires nearly 10 grid points per wavelength (Lombard et al., 2008), so the allowed grid size is about ∼1.2 m. For that the maximum coarsening value is $1.2\,\text{m}/0.15\,\text{m} \approx 8$. As this method allows us to take the coarsening value in the power of 2 only, we can use $\sigma = 2^3 = 8$. Therefore, we have carried out the simulation for $\sigma = 2^2 = 4$ and $\sigma = 2^3 = 8$ only, and compared the resulting seismograms for various

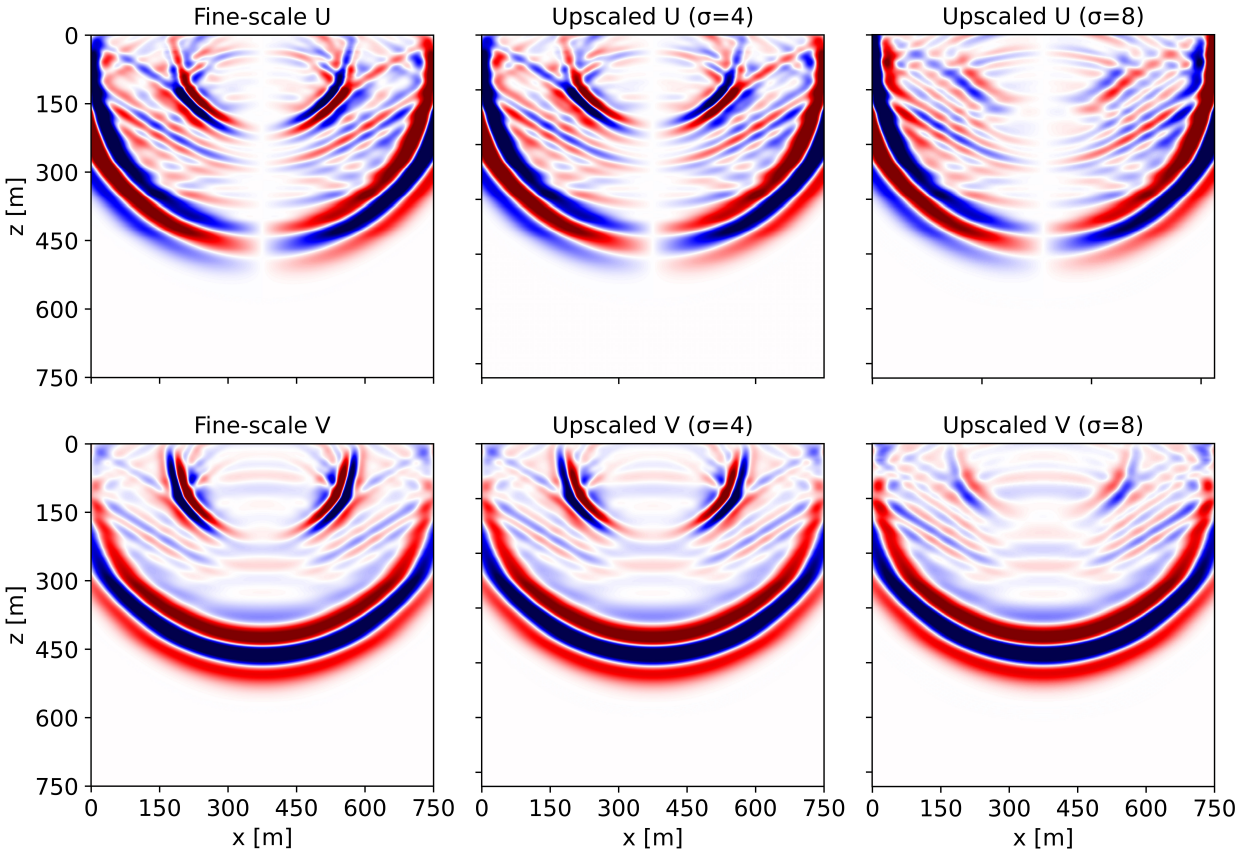

Figure 4: Comparison of Wavefield snapshots at $t = 0.1\,\mathrm{s}$ for horizontal (U) and vertical (V) components from the fine-scale and upscaled models.

central frequencies of the source wavelet (Figure 6).

The upscaled model's response is dependent on the frequency content of the wave traveling in the medium. For low frequencies, the response may not be affected, but for the higher frequencies, the response may differ from the original response. We have carried out wave simulation for various frequencies ($f_0 = 20, 30, 40$, and $50\,\mathrm{Hz}$) on the fine-scale model, and the upscaled Hempen model ($\sigma = 4, 8$).

The figure presents a component-wise (U and V) comparison of the fine-scale reference model (figure 2) and the upscaled models. For $\sigma = 4$, the upscaled model has a grid spacing of $0.6\,\mathrm{m}$ with 1250×1250 nodes, whereas for $\sigma = 8$, the grid spacing is $1.2\,\mathrm{m}$ with 625×625 nodes. The $\sigma = 4$ waveforms show excellent agreement with the fine-scale model across all frequencies, effectively preserving both long- and short-wavelength components through RG-based upscaling. In contrast, the $\sigma = 8$ model exhibits slight differences in amplitude and phase, reflecting the stronger smoothing inherent to this coarser upscaling. The close match for $\sigma = 4$ arises from its moderate upscaling factor, which retains more fine-scale heterogeneities critical for accurate wave propagation. For $\sigma = 8$, particularly at $50\,\mathrm{Hz}$, the amplitude differences and minor phase shifts are consistent with expectations from wavenumber approximation (Malkoti et al., 2022).

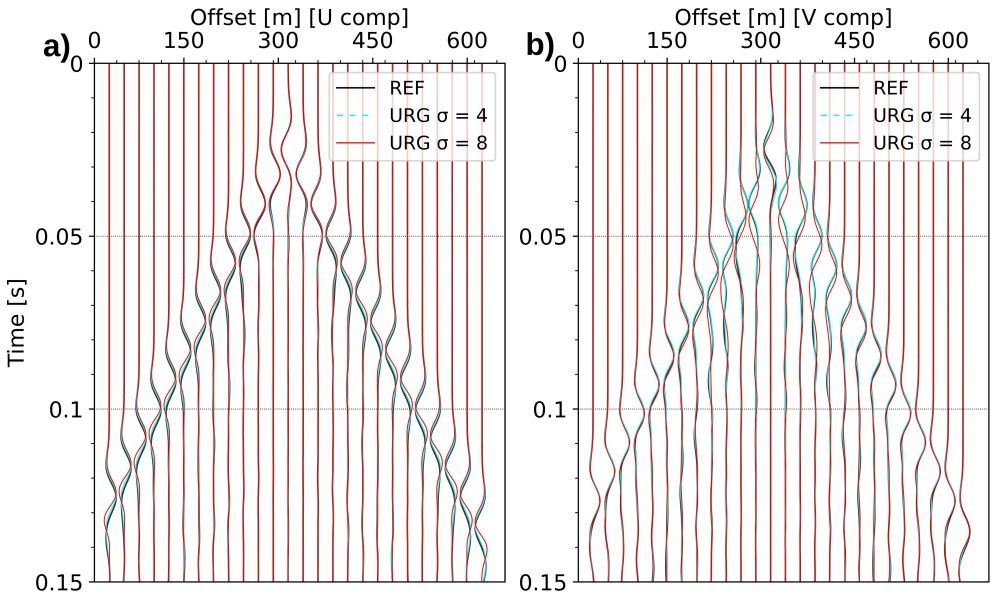

Figure 5: Superposition of synthetic waveforms is generated from the fine-scale Hempen model (black) and upscaled models are in cyan and red, respectively.

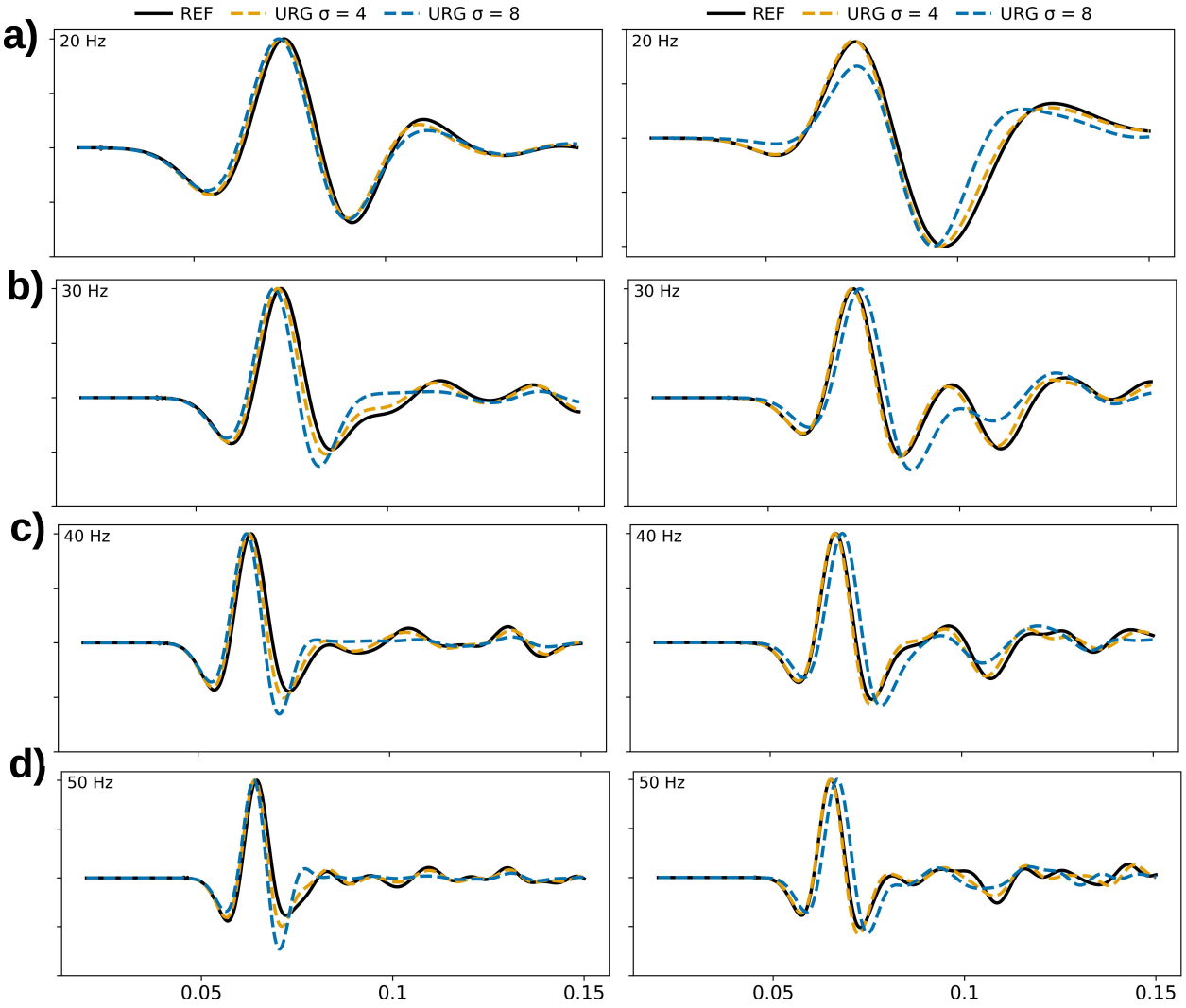

Figure 6: Comparison of waveforms between the fine-scale reference model (REF, black) and RG-theory-based upscaled models for different source frequencies. The left column shows the U component and the right column shows the V component of the wavefield. Panels (a)–(d) correspond to increasing central frequencies of 20 Hz, 30 Hz, 40 Hz, and 50 Hz, respectively.

3.2 Anticline Model

Anticline structure is an upwardly convex folded rock formation and it often serves as a potential zone for petroleum. The structure above it may have undergone a complex burial history, and thus, the top structure may have alternate sandy/shaly layers. Such a layered structure may result in anisotropy and thus may affect the travel time. To mimic a similar geological scenario, we generated a 2D anticline model (Figure 7). It has thick layers at the bottom and very thin layers at the top, having rapid variations and an anticlinal shape. Thick layers' velocities V_p vary between $2000\,\mathrm{m\,s^{-1}}$ and $6055\,\mathrm{m\,s^{-1}}$, with a velocity perturbation of $\pm 100\,\mathrm{m\,s^{-1}}$. The fine layer has alternate velocity variations of $1800\,\mathrm{m\,s^{-1}}$ and $2600\,\mathrm{m\,s^{-1}}$, respectively, with each layer thickness of approximately 3 m. The size of the model is 2560×2560 with a grid spacing of $\Delta h = 1$. The S-wave velocity model (V_s) is derived based on the assumed V_p/V_s ratio of 1.8. The elastic stiffness constants for the matrix are shown in the (Figure 7). Since the model is elastic, the stiffness tensor has $C_{11} = C_{33}$, and $C_{15} = C_{35} = 0$, and thereby the latter is not shown in the figure.

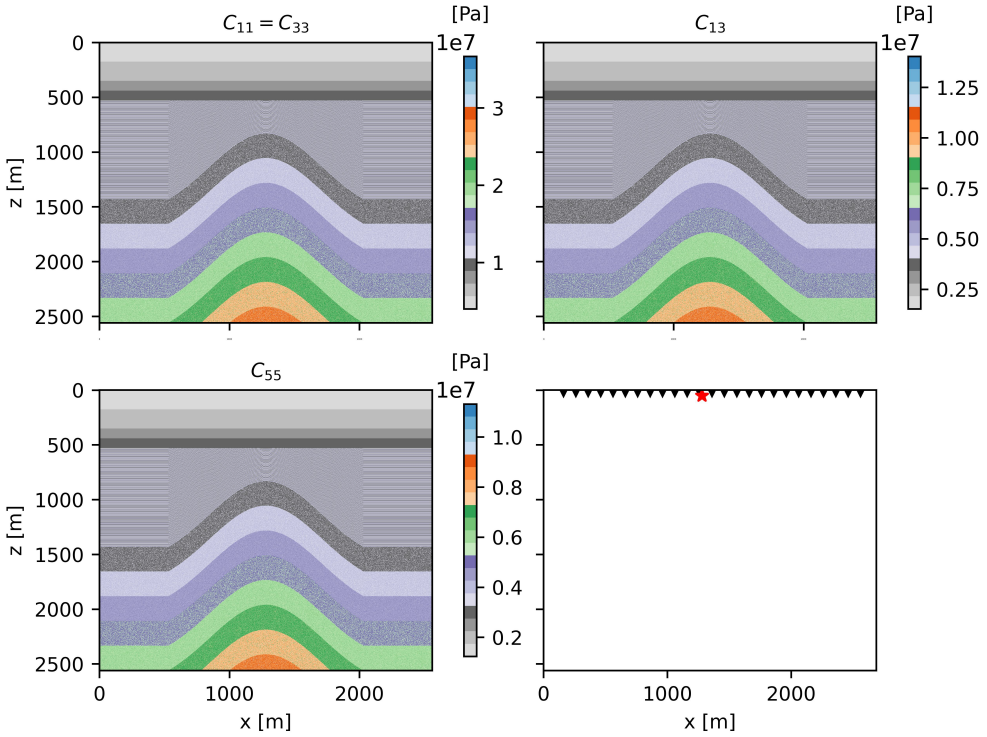

Figure 7: The components of the stiffness tensor C_{ij} of the fine-scale anticline model are shown. The right bottom image shows the arrangement for the source and receivers, where the source's location is indicated with a red star and the receiver's locations are indicated with black inverted triangles.

In this test, we used a Ricker wavelet with a central frequency of $f_0 = 15\,\mathrm{Hz}$, which contains significant frequency content up to approximately 24.55 Hz. In the anticline model, the minimum wavelength is $\sim 43\,\mathrm{m}$. The derivative operator requires nearly 10 grid points per wavelength (Lombard et al., 2008), so the allowed grid size is about $\sim 4.3\,\mathrm{m}$. We have selected coarsening ratios of $\sigma = 2$ and $\sigma = 4$, which resulted in upscaled models having 1280×1280 and 640×640 nodes, respectively. The stiffness tensor elements of the upscaled anticline model ($\sigma = 4$) are displayed in Figure 8.

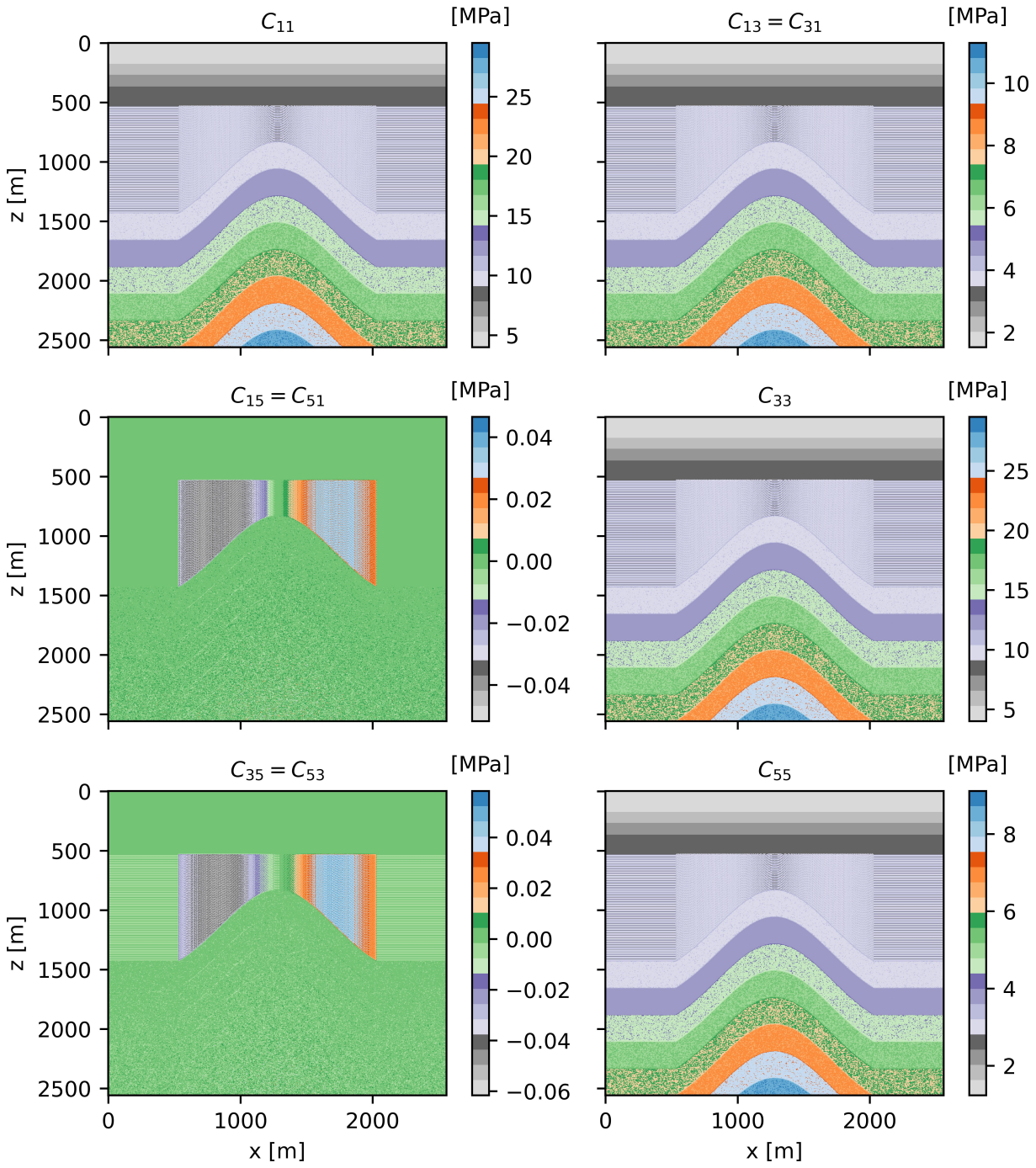

Figure 8: The stiffness tensor parameters of the upscaled anticline model ($\sigma = 4$). The panels represent C_{11}, C_{13}, C_{33}, C_{15}, C_{35}, and C_{55}, respectively.

It can be seen that in the upscaled model, $C_{11} \neq C_{33}$, and the components $C_{15} = C_{51}$ and $C_{35} = C_{53}$ are nonzero (Figure 8), while they are zero in the fine-scale model. The upscaled stiffness tensor components C_{11}, C_{33}, and C_{55} exhibit significant variations compared to their fine-scale counterparts.

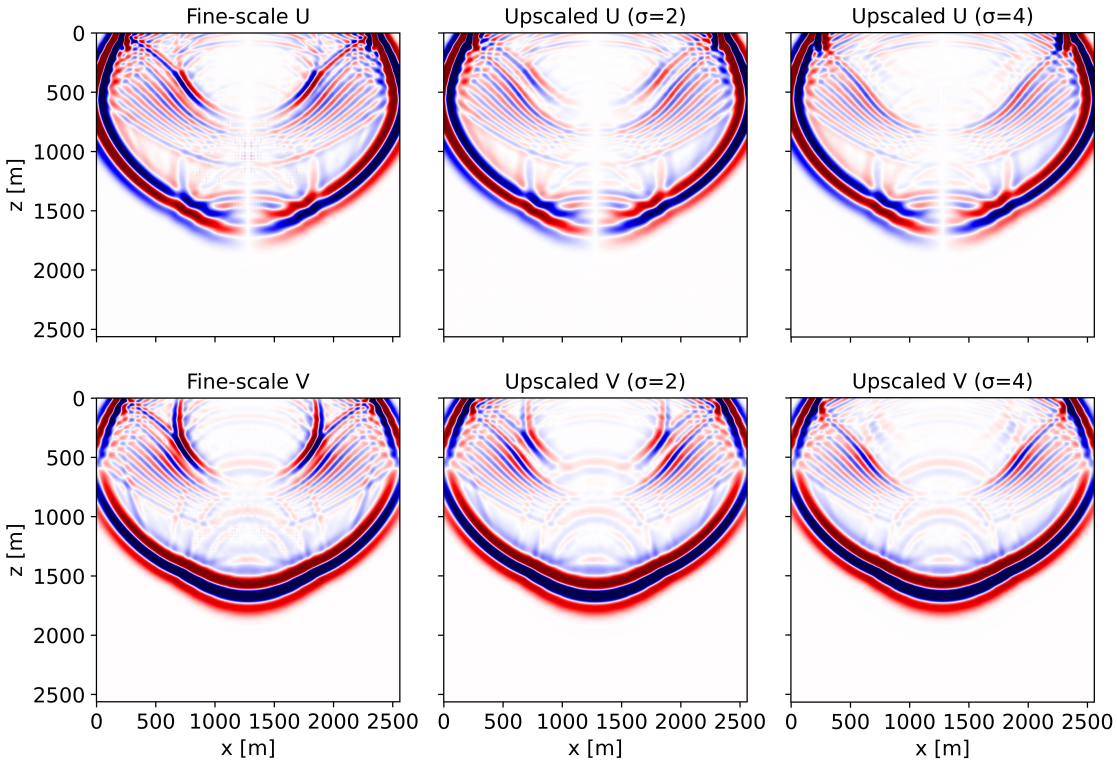

Figure 9: Comparisons of wavefield snapshots at $t = 0.6\,\mathrm{s}$ for the anticline model in both the fine-scale and upscaled models ($\sigma = 2$ and $\sigma = 4$)

.

We have compared the response of original and upscaled mediums by comparing the seismic wavefield in both the medium, following the same process explained for previous model. For both fine and upscaled models, we have used a Ricker wavelet with a central frequency of $f_0 = 15\,\mathrm{Hz}$ as a source which was placed near the surface at the center (laterally) of model. The grid spacing for the fine-scale and coarse scale models were 1 m,2m and 4 m, respectively. We employ a 2D rotated staggered grid finite-difference scheme for wave simulations in the fine-scale isotropic medium (with three independent stiffness tensor components) and the upscaled anisotropic media (with six independent components). The wavefield snapshots at $t = 0.6$ s for the horizontal (U) and vertical (V) components show direct wavefronts, strong reflections, and diffractions due to the model's complexity (Figure 9). The main wavefield features of the u and v components are well matched. However, the v component inner circle is visible in the fine-scale and upscaled model ($\sigma = 2$) but missing in the upscaled model ($\sigma = 4$), as the higher coarsening ratio homogenizes fine-scale heterogeneities to approximate effective macroscopic behavior. The surface-recorded seismograms (Figure 10) further assess the accuracy of the upscaling through the superposition of fine-scale (black, REF) and upscaled (cyan for $\sigma = 2$, red for $\sigma = 4$) waveforms. Differences in horizontal and vertical components are generally minor, indicating preservation of key seismic characteristics from the high-resolution model. The upscaled model with $\sigma = 2$ closely matches the fine-scale waveforms in both phase and amplitude, while the $\sigma = 4$ model exhibits slight deviations, particularly in amplitude. However, near-source locations show noticeable amplitude mismatches in the V component for $\sigma = 4$, likely due to the upscaling approximation of near-field effects and local heterogeneities, whereas at larger offsets, the waveforms align more closely. This alignment demonstrates the robustness of

RG-based upscaling for simulating wave propagation in anisotropic media derived from the complex anticline model.

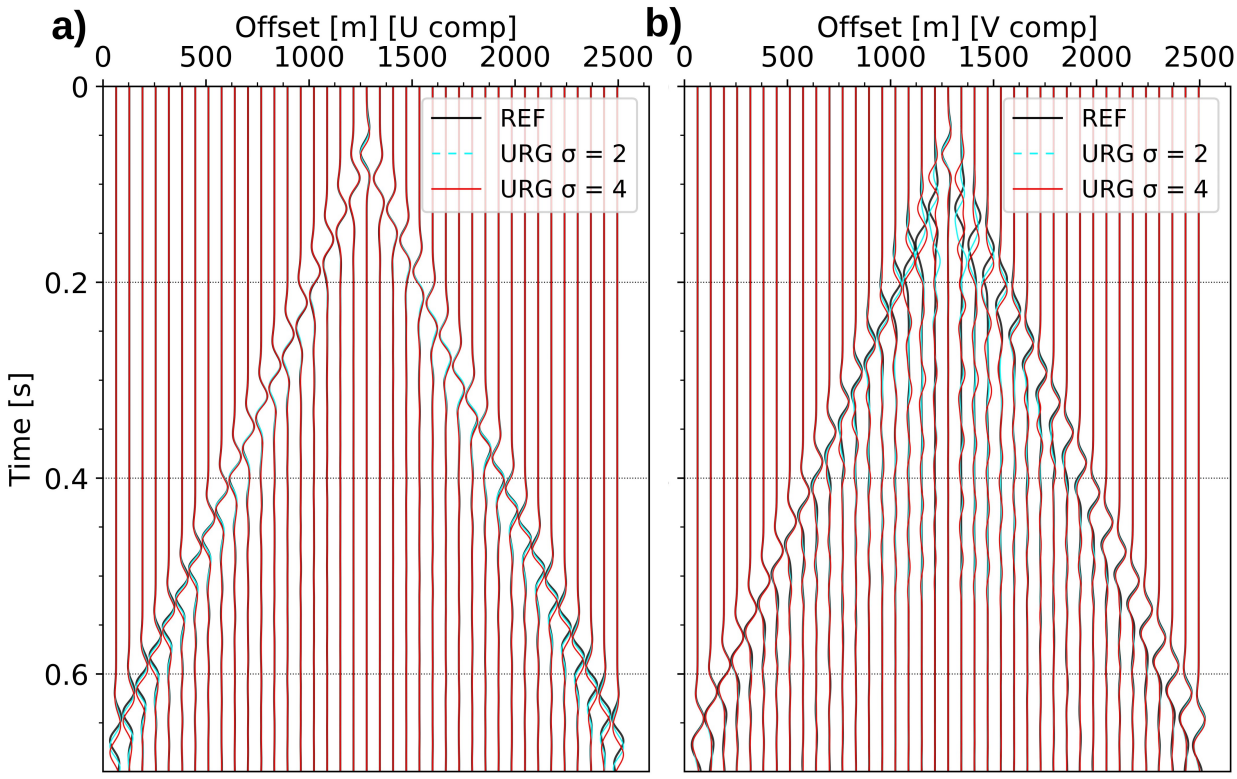

Figure 10: Superposition of synthetic waveforms computed for the anticline model, comparing the fine-scale (in black) and RG-theory based upscaled model (in cyan and red colors) solutions. Source and receiver positions are illustrated in Figure 7.

4 Conclusions

We presented a novel upscaling technique for the elastic wave equation that is based on Renormalization Group theory. It has an advantage in the context of upscaling the medium properties for the wave. The upscale medium is a coarser representation of the medium which is achieved by correcting the low-wavenumber model for higher wavenumbers. The limit of upscaling is dictated by the derivative operator, and within these limits, it should preserve kinematic as well as dynamic features of the wave. We have demonstrated it by carrying out upscaling for various coarsening levels and then running simulations for various source frequencies. Further, the upscaling values obtained using RG-theory are in agreement with the values obtained using Backus averaging. The RG upscaled model has been shown to have relatively higher variations corresponding to high wavenumbers, resulting in improved coarse-scale representations. The Hempens model and the Anticline model, both isotropic and elastic show the structural aniotropy after upscaling. The simulated wavefields and shotgather waveforms closely matched those of fine-scale simulations, indicating that the method reliably preserves essential seismic responses in structurally complex media. Overall, our results demonstrate that the RG-based upscaling framework offers a robust and accurate way to upscale the complex, heterogeneous elastic media while effectively preserving key seismic characteristics of

fine-scale structures, enabling accurate simulations on coarser grids.

Appendix A: Backus upscaling

The Backus averaging (Backus, 1962; Liner, 2014) is a well-established approach for computing effective elastic properties in layered media when layer thickness is much smaller than the seismic wavelength. It essentially provids an analytical representation of a complex layered system with a simplified average property. Backus upscaling requires the elastic velocities (V_p and V_s) and density (ρ) for each thin layer for computing equivalent anisotropic medium, i.e., transversely isotropic medium. This upscaled medium captures the long-wavelength behavior of wave propagation by effectively averaging the fine-scale heterogeneities. The effective stiffness coefficients (C_{11}, C_{33}, C_{13}, and C_{55}) at a coarser scale can be obtained using the following expressions.

$$C_{11} = \left\langle \frac{1}{\lambda + 2\mu} \right\rangle^{-1}, \tag{A-1}$$

$$C_{33} = 4\left\langle \frac{\mu(\lambda+\mu)}{\lambda + 2\mu} \right\rangle + \left\langle \frac{1}{\lambda + 2\mu} \right\rangle^{-1} \left\langle \frac{\lambda}{\lambda + 2\mu} \right\rangle^{2}, \tag{A-2}$$

$$C_{13} = \left\langle \frac{\lambda}{\lambda + 2\mu} \right\rangle \left\langle \frac{1}{\lambda + 2\mu} \right\rangle^{-1}, \tag{A-3}$$

$$C_{55} = \left\langle \frac{1}{\mu} \right\rangle^{-1} \tag{A-4}$$

Here, $\langle . \rangle$ represents a vertical moving average performed over a given window length, the λ and μ are the Lamé parameters that can be calculated using velocities as $\mu = \rho(V_p^2 - V_s^2)$, and $\lambda = \rho V_s^2$.

References

Backus, G. E., 1962, Long-wave elastic anisotropy produced by horizontal layering: Journal of Geophysical Research, **67**, 4427–4440.

Baysal, E., D. D. Kosloff, and J. W. Sherwood, 1983, Reverse time migration: Geophysics, **48**, 1514–1524.

Bensoussan, A., J.-L. Lions, and G. Papanicolaou, 1978, Asymptotic analysis for periodic structures: North-Holland.

Capdeville, Y., L. Guillot, and J.-J. Marigo, 2010, 2-d non-periodic homogenization to upscale elastic media for p–sv waves: Geophysical Journal International, **182**, 903–922.

Capdeville, Y., and J.-J. Marigo, 2007, Second order homogenization of the elastic wave equation for non-periodic layered media: Geophysical Journal International, **170**, 823–838.

Chammas, R., O. Abraham, P. Côte, H. A. Pedersen, and J. F. Semblat, 2003, Characterization of heterogeneous soils using surface waves: homogenization and numerical modeling: International Journal of Geomechanics, **3**, 55–63.

Cupillard, P., and Y. Capdeville, 2018, Non-periodic homogenization of 3-d elastic media for the seismic wave equation: Geophysical Journal International, **213**, 983–1001.

Fichtner, A., and S. M. Hanasoge, 2017, Discrete wave equation upscaling: Geophysical Journal International, **209**, 353–357.

Gao, K., E. T. Chung, R. L. Gibson Jr, S. Fu, and Y. Efendiev, 2015, A numerical homogenization method for heterogeneous, anisotropic elastic media based on multiscale theory: Geophysics, **80**, D385–D401.

Gibson Jr, R. L., K. Gao, E. Chung, and Y. Efendiev, 2014, Multiscale modeling of acoustic wave propagation in 2d media: Geophysics, **79**, T61–T75.

Gold, N., S. Shapiro, S. Bojinski, and T. Müller, 2000, An approach to upscaling for seismic waves in statistically isotropic heterogeneous elastic media: Geophysics, **65**, 1837–1850.

Guillot, L., Y. Capdeville, and J.-J. Marigo, 2010, 2-d non-periodic homogenization of the elastic wave equation: Sh case: Geophysical Journal International, **182**, 1438–1454.

Hanasoge, S., U. Agarwal, K. Tandon, and J. V. A. Koelman, 2017, Renormalization group theory outperforms other approaches in statistical comparison between upscaling techniques for porous media: Physical Review E, **96**, 033313.

Hanasoge, S. M., 2016, Spatio-spectral concentration of convolutions: Journal of Computational Physics, **313**, 674–686.

Jordan, T. H., 2015, An effective medium theory for three-dimensional elastic heterogeneities: Geophysical Journal International, **203**, 1343–1354.

Kormanikova, E., and K. Kotrasova, 2022, Micro-macro modelling of laminated composite rectangular reservoir: Composite Structures, **279**, 114701.

Levander, A. R., 1988, Fourth-order finite-difference p-sv seismograms: Geophysics, **53**, 1425–1436.

Liner, C. L., 2014, Long-wave elastic attenuation produced by horizontal layering: The Leading Edge, **33**, 634–638.

Lombard, B., J. Piraux, C. Gélis, and J. Virieux, 2008, Free and smooth boundaries in 2-d finite-difference schemes for transient elastic waves: Geophysical Journal International, **172**, 252–261.

Malkoti, A., S. M. Hanasoge, and R.-É. Plessix, 2022, Upscaling acoustic wave equation using renormalization group theory: Geophysics, **87**, T281–T290.

Malkoti, A., N. Vedanti, and R. K. Tiwari, 2018, An algorithm for fast elastic wave simulation using a vectorized finite difference operator: Computers & geosciences, **116**, 23–31.

Pratt, R. G., C. Shin, and G. Hick, 1998, Gauss–newton and full newton methods in frequency–space seismic waveform inversion: Geophysical journal international, **133**, 341–362.

Saenger, E. H., N. Gold, and S. A. Shapiro, 2000, Modeling the propagation of elastic waves using a modified finite-difference grid: Wave Motion, **31**, 365–373.

Tarantola, A., 1984, Inversion of seismic reflection data in the acoustic approximation: Geophysics, **49**, 1259–1266.

Vdovina, T., S. E. Minkoff, and S. M. Griffith, 2009, A two–scale solution algorithm for the elastic wave equation: SIAM Journal on Scientific Computing, **31**, 3356–3386.

Vidale, J. E., and R. W. Clayton, 1986, A stable free-surface boundary condition for two-dimensional elastic finite-difference wave simulation: Geophysics, **51**, 2247–2249.

Wang, Y., 2015, Frequencies of the ricker wavelet: Geophysics, **80**, A31–A37.

Zhang, O., and D. R. Schmitt, 2025, An optimized 2d/3d finite-difference seismic wave propagator using rotated staggered grid for complex elastic anisotropic structures: Computers and Geosciences, **196**, 105850.